

Electronic Supplementary Information

ZnO/ZnS heterostructure with enhanced interfacial lithium absorption for robust and large-capacity energy storage

Chenlong Dong,^{‡a,b} Xilin Zhang,^{‡c} Wujie Dong,^{‡b,d} Xueyu Lin,^b Yuan Cheng,^d Yufeng Tang,^d Siwei Zhao,^b Guobao Li^{*b} and Fuqiang Huang^{*bc}

^aSchool of Materials Science and Engineering, Tianjin University of Technology, Tianjin 300384, P.R. China

^bBeijing National Laboratory for Molecular Sciences and State Key Laboratory of Rare Earth Materials Chemistry and Applications, College of Chemistry and Molecular Engineering, Peking University, Beijing 100871, P.R. China

^cSchool of physics, Henan Normal University, Xinxiang 453007, P.R. China

^dState Key Laboratory of High Performance Ceramics and Superfine Microstructure, Shanghai Institute of Ceramics, Chinese Academy of Sciences, Shanghai 200050, P.R. China

[#]Chenlong Dong, XiLin Zhang and Wujie Dong contributed equally to this work.

*Corresponding author. E-mail: huangfq@pku.edu.cn (Fuqiang Huang),
liguobao@pku.edu.cn (Guobao Li)

S1. Experimental section

Materials preparation

Synthesis of ultrafine ZnS:OH: The synthesis procedure of ZnS:OH was based on the previous literature.^[1] Typically, 1 mmol Zn(OOCCH₃)₂·2H₂O and 1 mmol sublimed sulfur were suspended in 40 ml PEG-200 (polyethylene glycol) by stirring for 15 min and sonicating for 15 min. The suspension was stirred vigorously for 40 min at 180 °C and then cooled down naturally. The resultant light-yellow precipitation was separated by centrifugation at 8,000 rpm, washed four times by deionized water and ethanol, and dried at 70 °C overnight.

Synthesis of heterostructured ZnO/ZnS nanosheet: The ultrafine ZnS:OH was annealed in Ar atmosphere at 600 °C for 2 h.

Synthesis of ZnO: The ZnO/ZnS was annealed in muffle furnace at 440 °C for 12 h.

Synthesis of ZnS: 180 mg ZnO/ZnS was etched in 80 mL 2 M KOH solution for one hour at room temperature. The resultant ZnS was obtained by washed with deionized water and ethanol and dried at 70 °C overnight.

Characterizations

The crystal structures of prepared samples were investigated by X-ray diffraction (XRD) using a D2 Bruker X-ray diffractometer with Cu K α radiation ($\lambda = 1.5418 \text{ \AA}$) at a scanning rate of 2° min^{-1} in the 2θ range of $10\text{--}80^\circ$. The high-resolution PXRD data were collected on PANalytical X-Pert 3 X-ray diffractometer with Cu K α radiation ($\lambda_1 = 1.5405 \text{ \AA}$; $\lambda_2 = 1.5443 \text{ \AA}$) in the 2θ range of $5\text{--}120^\circ$. The Rietveld refinement was operated by GSAS software. X-ray photoelectron spectroscopy (XPS) was conducted to study the surface chemical environment and element valance state in an Axis Ultra spectrometer (Kratos Analytical) using Al K α radiation ($h\nu = 1486.7 \text{ eV}$). The obtained binding energy was calibrated using the C 1s peak at 284.8 eV of adventitious carbon as the criterion. Transmission electron microscopy (TEM) was performed to obtain the morphology, microstructure and composition in a JEM-2100F microscope (JOEL) with the ability to collect elemental information in HAADF-STEM mode. Raman spectra

were collected to acquire the chemical bond information by a DXRxi Micro Raman imaging spectrometer (Thermal Fisher) using an excitation laser with a wavelength of 532 nm. The Inductively coupled plasma-atomic emission spectrometer (ICP-AES) was performed on Prodigy 7 (Leeman, *Co. Ltd.*) under high-pressure Ar flow and the sample was treated by microwave digestion system. The thermogravimetric analysis-mass spectrometry (TG-MS) data were collected on TG-MS analyzer (labsys evolution, Setaram, *Co. Ltd.*) under Ar atmosphere from RT to 600 °C. Four-probe electronic conductivity measurement was performed on semiconductor powder resistivity tester (ST2722-SZ; Suzhou Jingge Electronic *Co. Ltd.*) to assess the electron conductivity of ZnO/ZnS, ZnO and ZnS.

For *ex-situ* TEM measurement, the collected electrode was immersed in dimethyl carbonate (DMC) and grounded into a powder-DMC slurry. The slurry was dipped onto a carbon-membrane-coated Cu-screen TEM holder, which was placed in a sealed container until TEM examination.

Electrochemical Measurement

The NMP (N-methyl-pyrrolidone) slurry consisting of active materials, acetylene black and polyvinylidene difluoride (PVDF) in a weight ratio of 8:1:1 was coated onto a copper foil by doctor-blade method. The obtained electrode was dried at 70 °C overnight and then cut into Φ 14 mm circular disks for subsequent battery assembly. Coin cells were assembled in a recirculating argon glovebox with the moisture below 0.1 ppm and oxygen content below 1 ppm. Lithium foil (China Energy Lithium) was used as the counter and reference electrode, and a glass fiber membrane (Whatman) was used as the separator, and the electrolyte used was 1 M LiPF₆ in ethyl carbonate (EC) and diethyl carbonate (DEC) (*w/w* = 50:50) with 10.0 % fluoroethylene carbonate (FEC) and 1.0 % vinylene carbonate (VC). The mass loading of the active materials was estimated to be *ca.* 0.9–1.0 mg cm⁻². Cyclic voltammetry was carried out on a CHI 760E electrochemical workstation at different scan rates. The charge–discharge tests and rate measurements were conducted on a LAND CT2001C battery system in the potential window of 0.01–3 V *vs.* Li/Li⁺ at different constant current densities. The

electrochemical impedance spectra (EIS) of the batteries were measured from 100 kHz to 0.01 Hz using a CHI760 E with an amplitude of 5 mV. Galvanostatic intermittent titration technique (GITT) was performed by discharging/charging in the range of 0.01–3 V for 30 min at 0.1 A g⁻¹ with a relaxation period of 60 min.

Coin cell ((+) LiCoO₂||prelithiated-ZnO/ZnS (-)) was assembled by applying LiCoO₂ cathode (180 mA h g⁻¹, maximum voltage 4.5 V) with the mass loading of *ca.* 7.5 mg cm⁻², and ZnO/ZnS anode (*ca.* 1200 mA h g⁻¹) with the mass loading of *ca.* 1.1 mg cm⁻². The N/P ratio is *ca.* 1. Both the anode and cathode were cut into Φ 12 mm circular disks for subsequent battery assembly. The ZnO/ZnS anode was prelithiated by an electrochemical method reported by Tobias Placke *et al.*^[2] The electrolyte was bought from the DodoChem (high voltage 5 V electrolyte, LB-111). The separator was the PP membrane. The optimal working voltage is 1–4.2 V.

Pouch cell ((+) LiCoO₂ || ZnO/ZnS (-)) was assembled by applying double-sided LiCoO₂ cathode (180 mA h g⁻¹, maximum voltage 4.5 V) with the mass loading of *ca.* 7.5 mg cm⁻² (single side), and double-sided ZnO/ZnS anode (~1200 mA h g⁻¹) with the mass loading of *ca.* 1.24 mg cm⁻² (single side). The N/P ratio is *ca.* 1.1. Both the anode and cathode were cut into 70 mm×35 mm rectangles with reserved battery tab for subsequent battery assembly. The electrolyte was bought from the DodoChem (high voltage 5 V electrolyte, LB-111). The separator was the PP membrane. The pouch cell is encapsulated by aluminum-plastic film. The optimal working voltage is 1–3.5 V.

Computational Details

The spin polarized periodic density functional theory calculations were performed using the Vienna Ab-initio Simulation Package (VASP) code.^[3] For improving the calculation efficiency, core electrons were replaced by the projector augmented wave (PAW) pseudo-potentials.^[4] The generalized gradient approximation of the Perdew, Burke, and Ernzerhof (PBE) functional^[5] was utilized for the exchange and correlation. The wave functions were expanded in plane waves with a cut off energy of 450 eV. The convergence criterion for the electronic self-consistent iteration was set to

10^{-5} eV, and the maximum force on each atom was less than 0.05 eV \AA^{-1} . The Brillouin zone was sampled with a single K point at Γ -centered for saving the computational time. In current simulation, the adsorption energy is calculated by the expression: $E_{\text{ads}} = E_{\text{A/B}} - E_{\text{A}} - E_{\text{B}}$, in which the $E_{\text{A/B}}$ and E_{A} (E_{B}) stand for the adsorbed and isolated system, respectively. The vacancy formation energies are calculated by the equation: $E_{\text{form}} = E_{\text{v/S}}^* + E^* - E_{\text{S}}$, where the $E_{\text{v/S}}^*$ and E_{S} stand for the systems with and without vacancy, respectively. The E^* is energy of the single sulfur or oxygen atom.

S2. Figures and tables

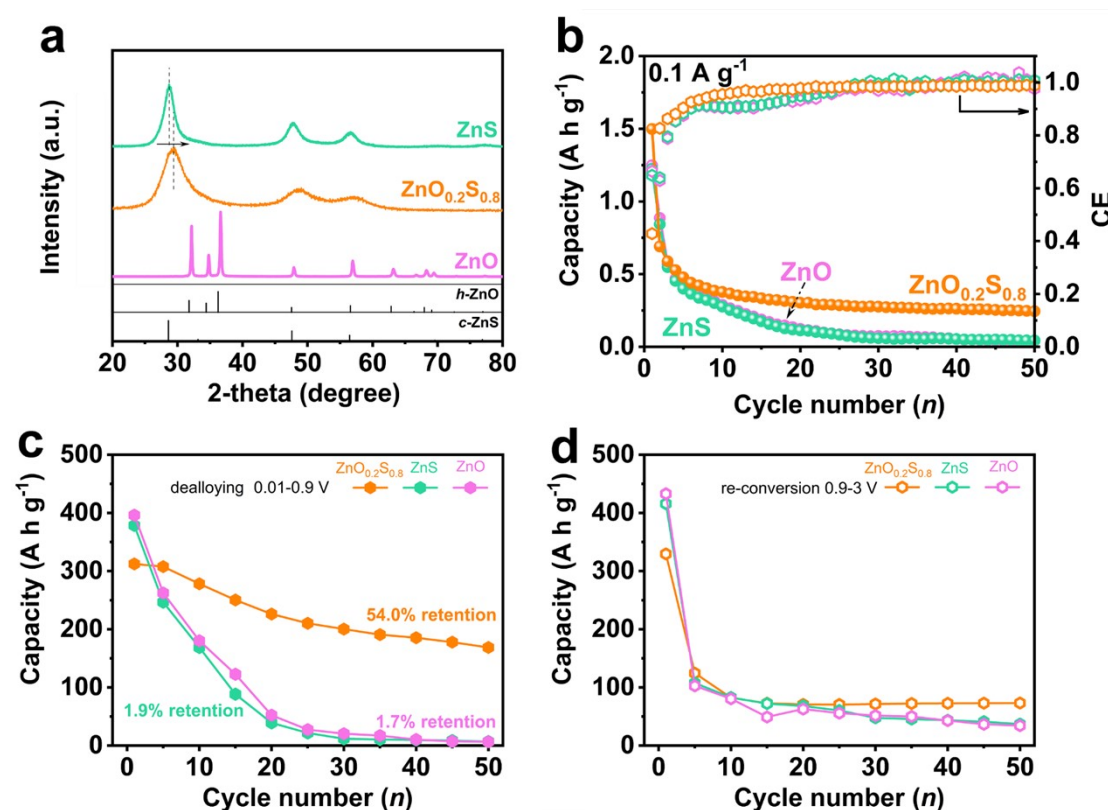
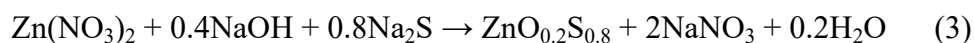
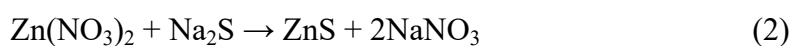


Fig. S1. (a) XRD patterns of ZnO, ZnS and ZnO_{0.8}S_{0.2}. (b) Cyclic performance of ZnO, ZnS and ZnO_{0.8}S_{0.2} at 0.1 A g⁻¹. The capacity contributed by (c) dealloying process (0–0.9 V) and (d) re-conversion process (0.9–3 V).

Preliminary experimental:

ZnO, ZnS and ZnO_{0.2}S_{0.8} were prepared by facile precipitation method according to the following equations:



The obtained precipitates are annealed at 400 °C for 2 h under Ar flow.

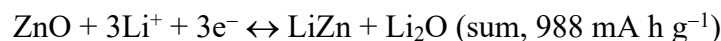
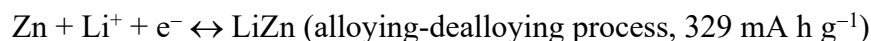
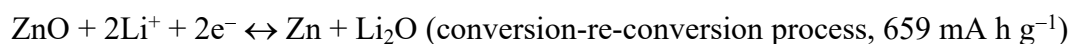
Results and discussion of preliminary experimental:

The XRD patterns (Fig. S1a) confirms the successful preparations of hexagonal ZnO and cubic ZnS. For ZnO_{0.8}S_{0.2}, the peak location shifts into high degree due to the radius difference of O²⁻ (0.14 nm) and S²⁻ (0.18 nm).

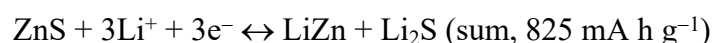
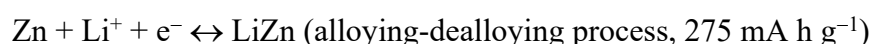
The reaction mechanisms of ZnO, ZnS and ZnO_{0.8}S_{0.2} are summarized as following

equations:

(1) ZnO



(2) ZnS



(3) ZnO_{0.2}S_{0.8}

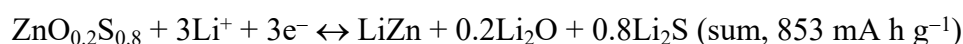
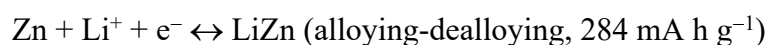
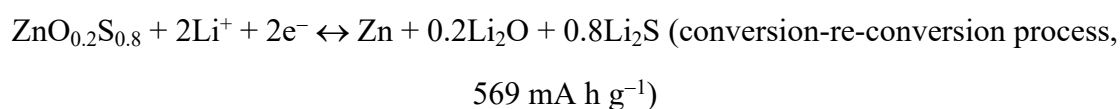


Fig. S1b presents the cyclic performance of ZnO, ZnS and ZnO_{0.8}S_{0.2} at 0.1 A g⁻¹. Although three samples experience conspicuous capacity fading, heteroanionic ZnO_{0.8}S_{0.2} anode displays highest capacity (245 mA h g⁻¹) and best stability among three samples, confirming the feasibility of heteroanion tuning.

According to previous report [6], the charging capacity can be divided into two parts: dealloying (0.01–0.9 V) and re-conversion process (0.9–3 V), as shown in **Fig. S1c** and **S1d**. For dealloying process, the capacity of ZnO_{0.2}S_{0.8} is 168.7 mA h g⁻¹ with 54.0 % retention, while capacities for ZnO and ZnS can be neglected. Such results confirm that the sole Li₂O matrix in ZnO electrode and Li₂S matrix in ZnS electrode cannot avoid the Zn agglomeration. While in ZnO_{0.2}S_{0.8} electrode, the Li₂O/Li₂S hybrid matrix can effectively relieve Zn agglomeration. For re-conversion process, these three electrodes fade rapidly due to weak electron conductivity, even so, the re-conversion capacity of ZnO_{0.2}S_{0.8} is still highest.

The preliminary experimental results illustrate that the Li₂O/Li₂S can keep Zn from agglomeration. However, the capacity of this ZnO_{0.2}S_{0.8} electrode is much low than the theoretical capacity.

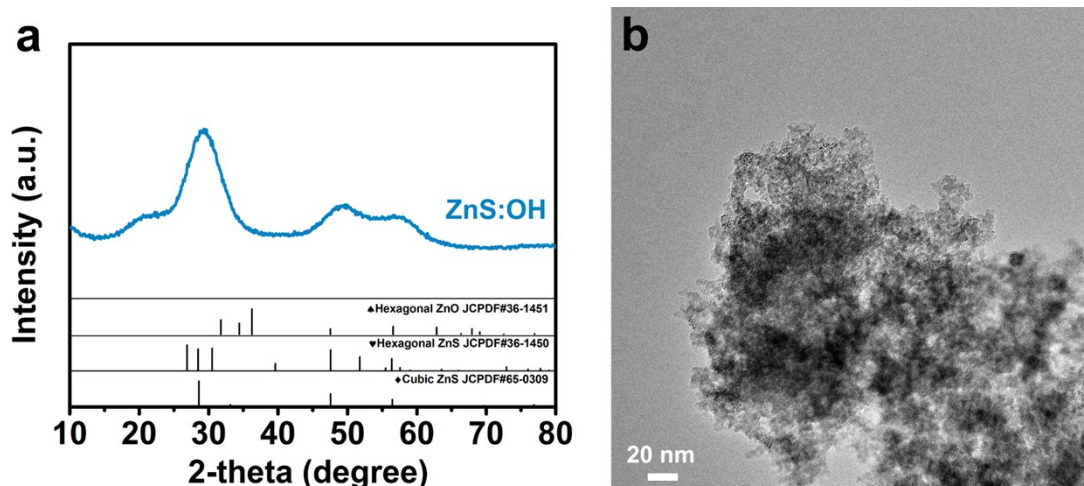


Fig. S2. (a) XRD patterns of ZnS:OH. **(b)** Low-resolution TEM image of ZnS:OH.

The ZnS:OH crystallizes in blende-type ZnS (PDF#65-0309) with a crystalline size of *ca.* 5 nm according to the Scherrer equation ($D=K\gamma/B\cos\theta$, $K=0.89$, $\gamma=0.154$ nm, $B=5.633/\pi$, $\theta=29.188^\circ$) for (111) peak. The morphology and particle size are also investigated by TEM, suggesting the grain size of *ca.* 5 nm nanodots.

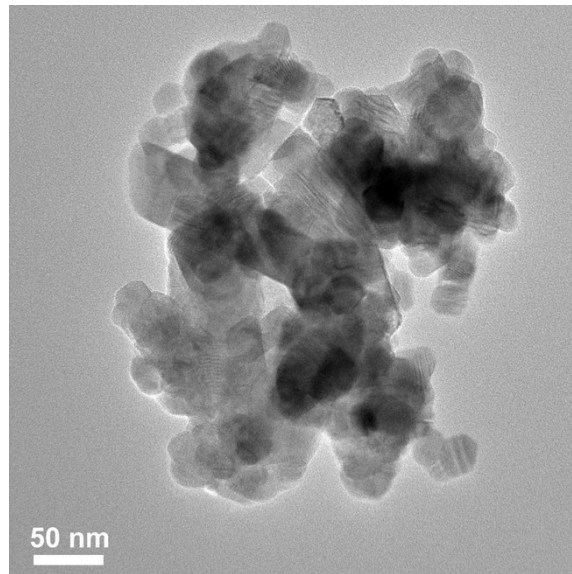


Fig. S3. Low-resolution TEM image of ZnO/ZnS.

The ZnS:OH nanodots grew into ZnO/ZnS nanosheets after Ar annealing.



Fig. S4. EDX analysis of ZnO/ZnS nanosheets under HAADF-STEM mode.

The atomic ratio of Zn/O/S is semi-quantificationally confirmed as 1:0.2:0.8 according to the EDX analysis.

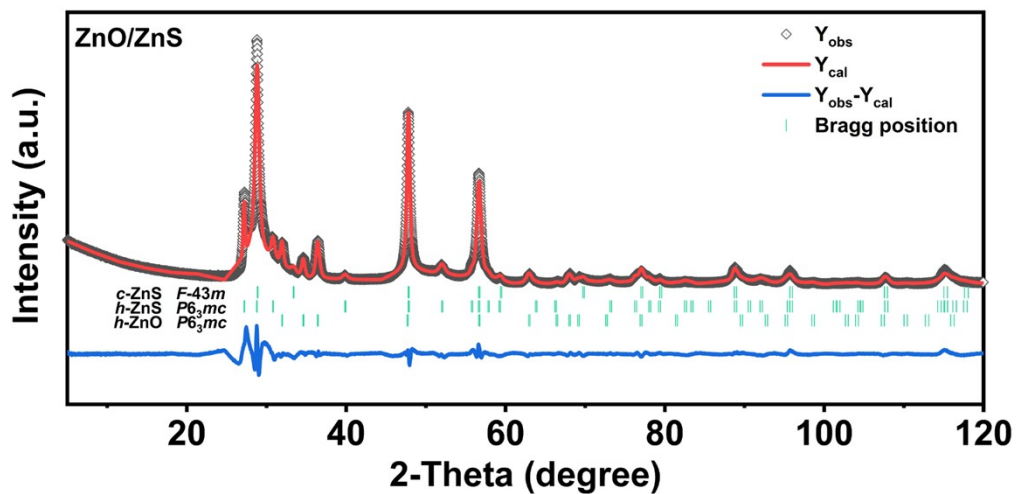


Fig. S5. Rietveld refined XRD patterns of ZnO/ZnS heterostructure.

The Rietveld refinement of XRD pattern confirms that the ZnO/ZnS heterostructure is composed of *h*-ZnO, *h*-ZnS and *c*-ZnS.

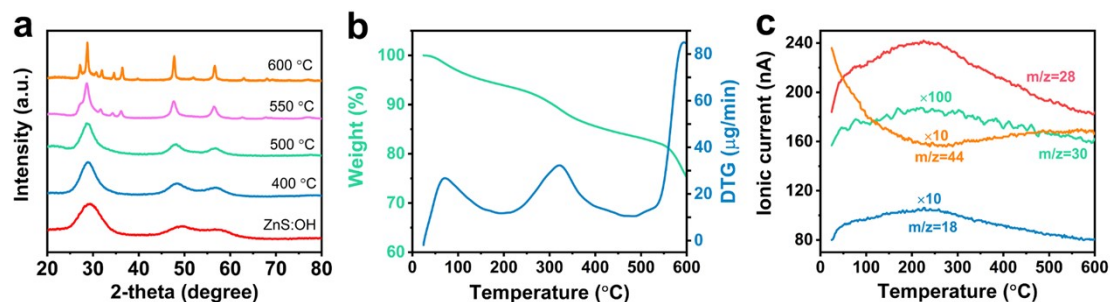


Fig. S6. (a) The XRD pattern of ZnS:OH annealing at different temperature for 2 h. (b) TG and (c) MS curves of ZnS:OH.

The XRD patterns of ZnS:OH at different annealing temperature for 2 h shows the effect of the H elimination on the final product (**Fig. S6a**). From RT to 500 °C, the crystalline phase is mainly cubic ZnS without any impurities except that the crystallinity is enhanced. After the annealing temperature increases to 550 °C, the XRD result of the product reveal that there are large amount of cubic ZnS (*c*-ZnS, JCPDF#65-0309; $F\bar{4}3m$, $a=b=c=5.409$ Å; $\alpha=\beta=\gamma=90^\circ$), small amount of hexagonal ZnS at 28° (*h*-ZnS, JCPDF#36-1450; $P6_3mc$, $a=b=3.821$ Å, $c=6.257$ Å; $\alpha=\beta=90^\circ$, $\gamma=120^\circ$) and very small amount of hexagonal ZnO (JCPDF#36-1451; $P6_3mc$, $a=b=3.250$ Å, $c=5.207$ Å; $\alpha=\beta=90^\circ$, $\gamma=120^\circ$). With increasing the temperature up to 600 °C, partial cubic ZnS is converted into hexagonal ZnS.

In order to confirm the form of H element elimination, the TG-MS was carried out on the ZnS:OH sample from RT to 600 °C under Ar flow at the same time (**Fig. S6b-c**). The MS curves show some humps for $m/z=18$ (H_2O), $m/z=28$ (C_2H_4), and $m/z=30$ ($HCHO$). The C_2H_4 and $HCHO$ may be from the decomposition of PEG residuals. The hump for $m/z=18$ (H_2O) is owned as the dehydration between two neighboring $-OH$ groups. The $m/z=44$ signal decreases from RT to 200 °C, which can be ascribed as the removal of CO_2 removing. The following signal increasement from 200 to 600 °C may be derived from the C_2H_4O (oxirane) generation.

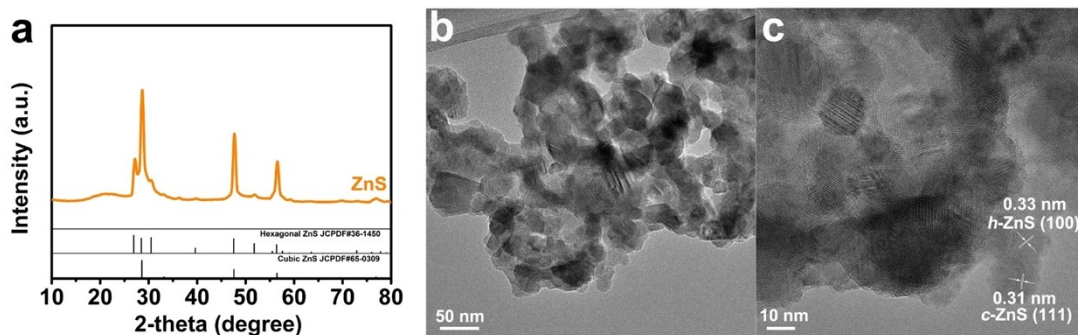


Fig. S7. (a) XRD pattern, (b) LR-TEM image and (c) HR-TEM image of ZnS.

The pure ZnS was prepared by alkaline-etching of as-prepared ZnO/ZnS heterostructure. The XRD pattern confirms the co-existence of hexagonal ZnS (JCPDF#36-1450) and cubic ZnS (JCPDF#65-0309) without the occurrence of ZnO phase. The LR-TEM image manifests the nanosheet morphology, and the HR-TEM image can further confirm the ZnS phase.

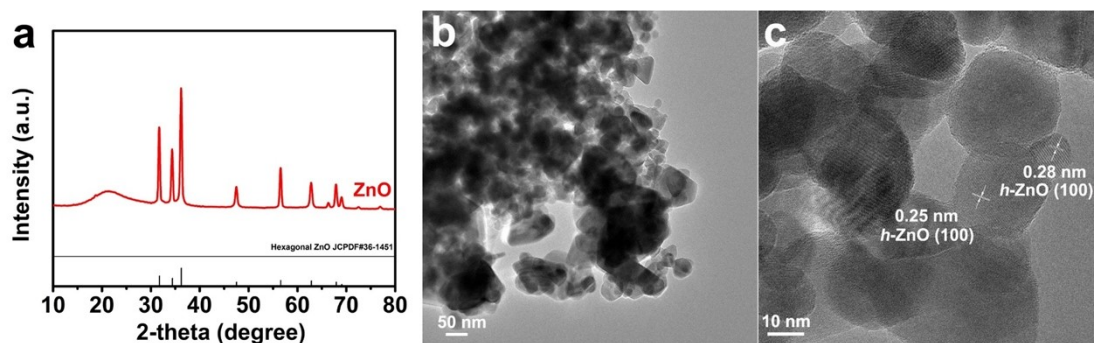


Fig. S8. (a) XRD pattern, (b) LR-TEM image and (c) HR-TEM image of ZnO.

The pure ZnO was prepared by air-calcination of as-prepared ZnO/ZnS heterostructure. The XRD pattern confirms the existence of hexagonal ZnO (JCPDF#36-1451) without the occurrence of ZnS phase. Similarly, the LR-TEM image manifests the nanosheet morphology, and the HR-TEM image can further confirm the ZnO phase.

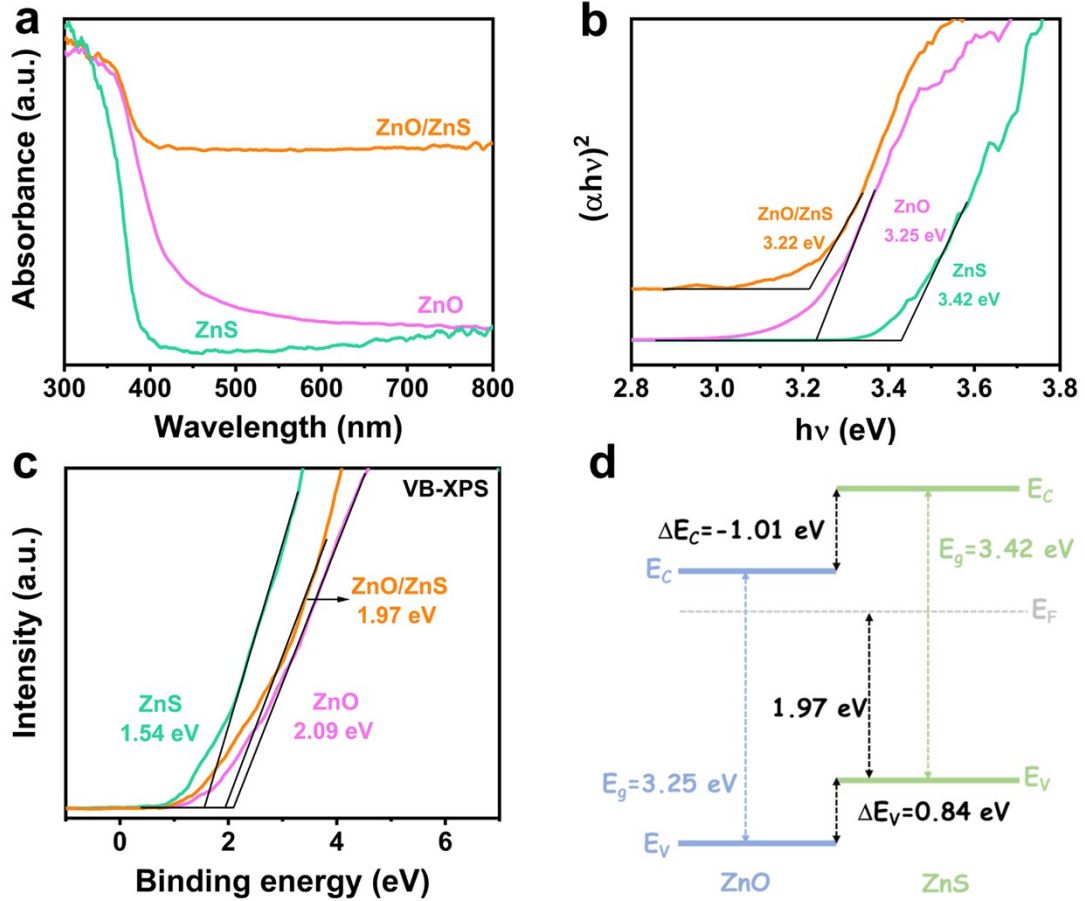


Fig. S9. (a) UV-vis spectra and (b) band gap calculations and (c) VB-XPS of ZnO, ZnS and ZnO/ZnS. (d) The schematic of the band alignment for the ZnO/ZnS.

The valence band (VB), conduction band (CB), band gap (E_g) had been confirmed by VB-XPS, XPS and UV-vis, as shown in **Fig.S9a-c**. The valence band offset (VBO, ΔE_v) and conduction band offset (CBO, ΔE_c) are calculated as following:

$$\Delta E_v = (E_{O\ 1s}^{ZnO/ZnS} - E_{S\ 2p3/2}^{ZnO/ZnS}) - (E_{O\ 1s}^{ZnO} - E_{VBM}^{ZnO}) + (E_{S\ 2p3/2}^{ZnS} - E_{VBM}^{ZnS})$$

$$\Delta E_c = (E_g^{ZnO} - E_g^{ZnS}) - \Delta E_v$$

According to above equation, the ΔE_v and ΔE_c are calculated as 0.84 eV and -1.01 eV, respectively. Thus, the schematic of the band alignment for the ZnO/ZnS has been drawn, as shown in **Fig. S9d**, which suggests that the ZnO/ZnS heterostructure is II-type alignment.

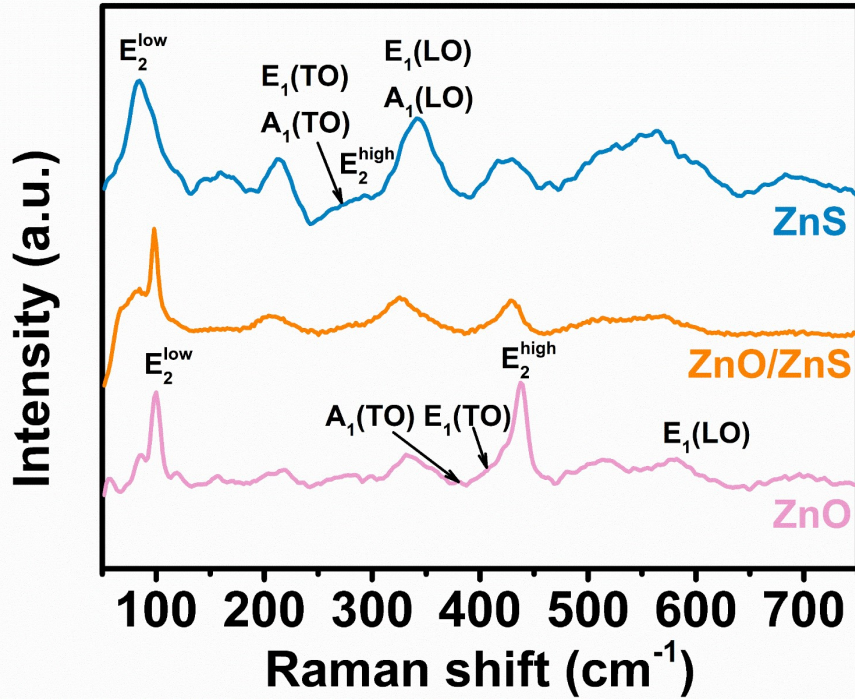


Fig. S10. Raman shift of ZnO, ZnS and ZnO/ZnS heterostructure.

To further confirm the interaction of ZnO/ZnS heterostructure, the Raman spectra had been investigated. Two fundamental peaks can be observed at 100 and 438 cm^{-1} in pure ZnO material, corresponding to the E_2^{low} and E_2^{high} mode respectively. Moreover, the most intensive second-order mode at 331 cm^{-1} , can be ascribed to difference $E_2^{\text{high}} - E_2^{\text{low}}$. In pure ZnS, the peaks located at 84 cm^{-1} and the weak broader peaks at 290 cm^{-1} can be attributed to the E_2^{low} and E_2^{high} of ZnS. Notably, the Raman peaks of ZnO/ZnS are relatively broader than that of pure ZnO and ZnS, owing to the interaction between ZnO and ZnS and defects around interface.

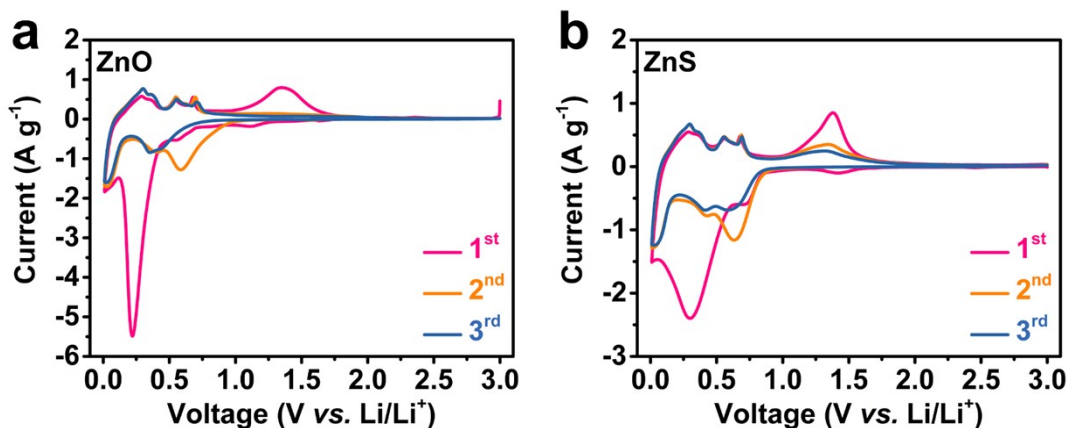


Fig. S11. CV curves of (a) ZnO and (b) ZnS.

During the first cathodic scan, the peak within 0.5–1.0 V can be owned as conversion reaction to generate the Zn nanodomains and $\text{Li}_2\text{O}/\text{Li}_2\text{S}$ matrix. A peak at *ca.* 0.2–0.3 V can be attributed to the formation of LiZn nanoalloys together with the decomposition of electrolyte. In subsequent anodic sweep, the continuous peaks at *ca.* 0.30, 0.54 and 0.70 V confirmed the multistep delithiation process of LiZn: $\text{LiZn} \rightarrow \text{Li}_2\text{Zn}_3 \rightarrow \text{LiZn}_2 \rightarrow \text{Li}_2\text{Zn}_5 \rightarrow \text{Zn}$. The broader peaks at 1.40 V can be related to the oxidation of Zn^0 to Zn^{2+} . While for ZnO and ZnS, the CV curves whether for conversion or alloying reaction fade quickly, demonstrating the highly irreversible lithium storage. The cyclic stability of ZnO (or ZnS) is much lower than that of ZnO/ZnS heterostructure.

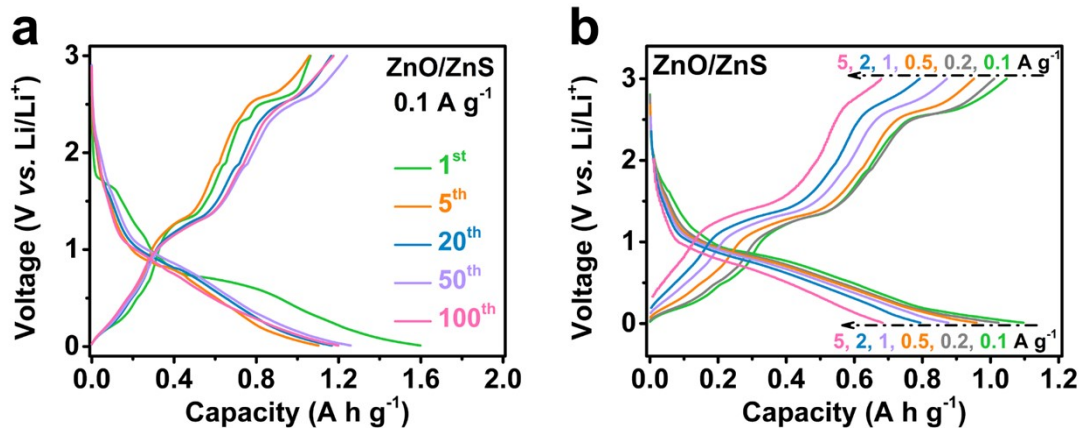


Fig. S12. (a) Galvanostatic charge–discharge curves at 0.1 A g⁻¹ of ZnO/ZnS heterostructure. (b) Rate charge–discharge curves of ZnO/ZnS heterostructure from 0.1 to 5 A g⁻¹.

Figure S12a: The irreversible capacity locates between 0.6 to 0.1 V due to electrolyte decomposition on active Zn nanodomains.

Figure S12b: Rate capacities of *ca.* 1098, 1024, 959, 876, 794 and 683 mA h g⁻¹ for ZnO/ZnS electrode can be harvested under the current densities of 0.1, 0.2, 0.5, 1, 2 and 5 A g⁻¹, respectively.

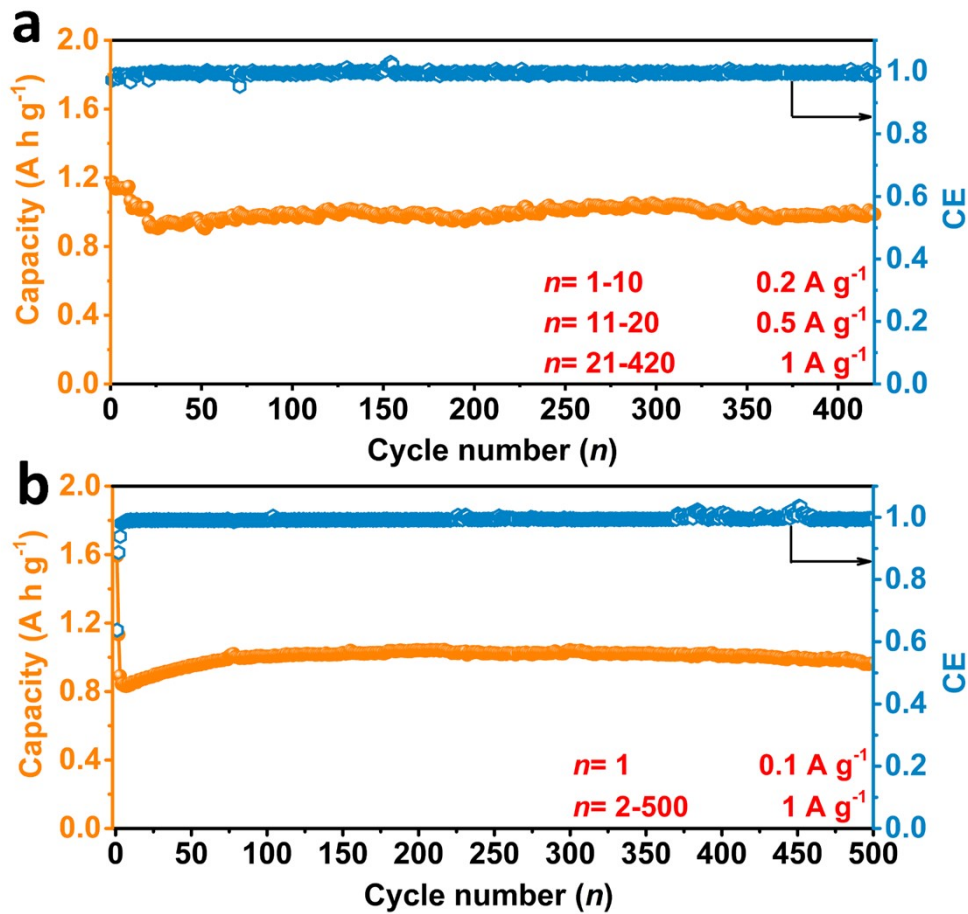


Fig. S13. (a) Long-term cyclic performance at 1 A g⁻¹ tested after rate measurement (1st-10th: 0.2 A g⁻¹; 11th-20th: 0.5 A g⁻¹; 21st-420th: 1 A g⁻¹). **(b)** Long-term cyclic performance at 1 A g⁻¹ with the 1st activation at 0.1 A g⁻¹.

Following the short-cycle rate performance test, we adopted the same integrated battery to investigate the long-term stability (Figure S13a). Although the battery has been tested by high-rate of 5 A g⁻¹, it can also deliver a capacity of 964.2 mA h g⁻¹ at 1 A g⁻¹ after 400 cycles. Compared with the model of moderate current rising, the severe model had been employed as shown in Figure S13b—0.1 A g⁻¹ at the 1st cycle and 1 A g⁻¹ from the 2nd to 500th cycle. The ZnO/ZnS can maintain 997.5 mA h g⁻¹ after 500 cycles, which is approximately equal to the discharge capacity in Figure S13a. In this tested model, the capacity comes through the ‘negative fading’, which can be considered as the phase/structure-reconstruction process.

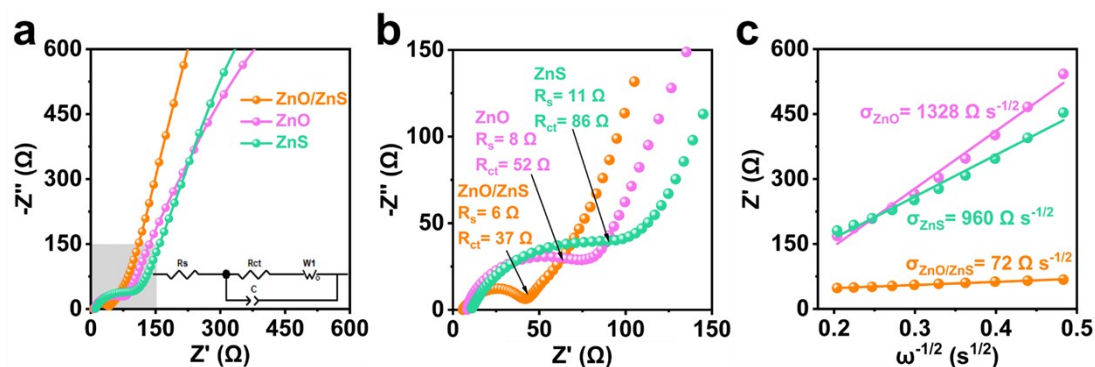


Fig. S14. Electrochemical impedance spectroscopy (EIS) analysis. (a) Nyquist plot at the OCV after the 1st cycle (amplitude: 5 mV) and the corresponding fitting equivalent circuit. (b) Amplified Nyquist plot of shadow region in (a). (c) The corresponding Z' vs. $\omega^{-1/2}$ plot.

The four-probe electron conductivity measurement was performed on semiconductor powder resistivity tester to assess the electron conductivity of ZnO/ZnS, ZnO and ZnS. The electron conductivities of ZnO/ZnS, ZnO and ZnS are 1.2×10^{-3} , 1.1×10^{-4} and $7.4 \times 10^{-5} \text{ S cm}^{-1}$, respectively.

The electrochemical impedance spectroscopy (EIS) had been carried out, as shown in **Fig. S14a** and the corresponding parameter is fitted by Zview software. The intercept at the real impedance axis in the high-frequency region corresponds to the ohmic resistance (R_s), which is related to the total ohmic impedance of electrolyte, separator and active materials. The R_s of ZnO/ZnS electrode is 6Ω , which is smaller than that of ZnO ($R_s = 8 \Omega$) and ZnS ($R_s = 11 \Omega$). The semicircle in the middle-high frequency region can be assigned to be charge transfer resistance (R_{ct} , electrochemical reaction resistance). The straight line in the low frequency region (Warburg impedance) is associated with the lithium diffusion process within active material particle. To conveniently compare the charge transfer ability, the shadow region in **Fig. S14a** has been amplified, as depicted in **Fig. S14b**. Conspicuously, the ZnO/ZnS electrode manifests the smallest R_{ct} value (37Ω), which is much lower than that of ZnO ($R_{ct} = 52 \Omega$) and ZnS ($R_{ct} = 86 \Omega$), indicating the higher electrochemical activity and the faster charge-transfer process of ZnO/ZnS electrode. Besides, the diffusion coefficient of Li^+ can be estimated by the following formula:

$$D_{Li^+} = \left(\frac{RT}{\sqrt{2}\sigma ACn^2F^2} \right)^2 = \frac{R^2T^2}{2\sigma^2A^2C^2n^4F^4} \quad (1)$$

Where R is the gas constant, T is the absolute temperature, A is the area of electrode, C is the volumetric concentration of Li⁺, n is the number of electron transfer and F is the Faradic constant. The σ is the Warburg coefficient which is connected with real part of impedance Z' obeying following equation:

$$Z' = R_s + R_{ct} + \sigma\omega^{-\frac{1}{2}} \quad (2)$$

The σ can be obtained by calculating the slope of Z' (real part of impedance) against ω^{-1/2} (the reciprocal of square root of angular frequency, ω= 2πf) plot, as shown in **Fig. S14c**. The σ-value of ZnO/ZnS, ZnO and ZnS is 72, 1328 and 960 Ω s^{-1/2}, respectively.

According to eqn. (1), the calculated D_{Li^+} of ZnO/ZnS is 1.27×10⁻¹³ cm² s⁻¹, which is 584-folds higher than that of ZnO ($D_{Li^+} = 2.17 \times 10^{-16}$ cm² s⁻¹) and 211-folds higher than that of ZnS ($D_{Li^+} = 6.01 \times 10^{-16}$ cm² s⁻¹), confirming the excellent Li⁺ conductivity of ZnO/ZnS. Moreover, the EIS plot of ZnO/ZnS exhibits linearity with a slope close to 90° in the low frequency region, indicating a characteristic of capacitive property.

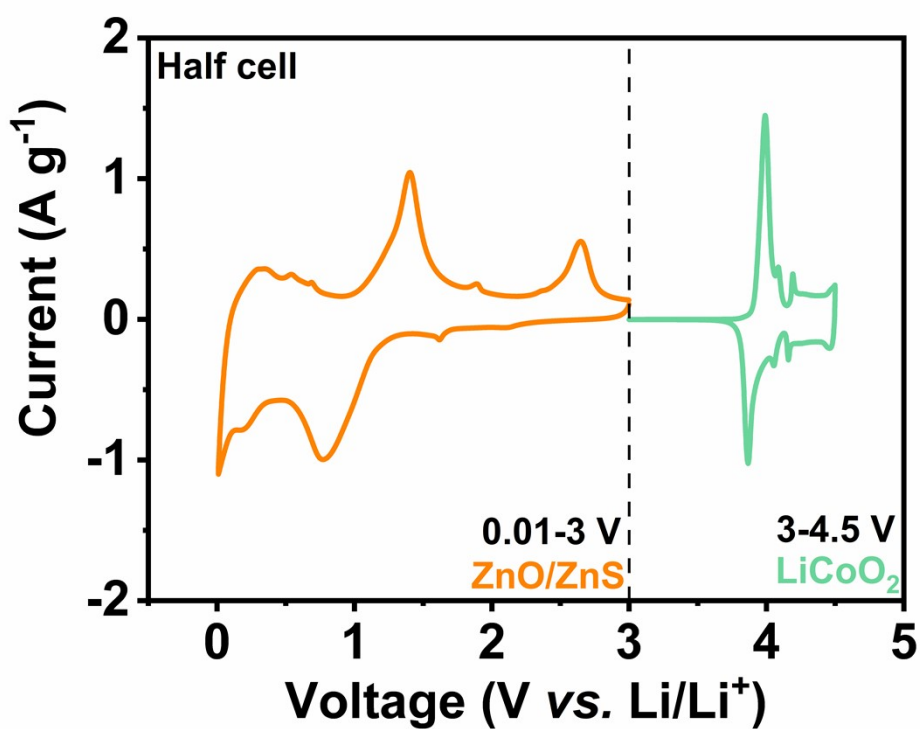


Fig. S15. CV profiles of half-cell LiCoO₂ cathode and half-cell ZnO/ZnS anode.

To verify the practical application of the ZnO/ZnS heterostructure, a coin-type full cell with the ZnO/ZnS anode and high-voltage (4.5 V) LiCoO₂ cathode, was assembled and tested. The CV curves of ZnO/ZnS and LiCoO₂ half-cell were investigated to confirm potential window of full cell.

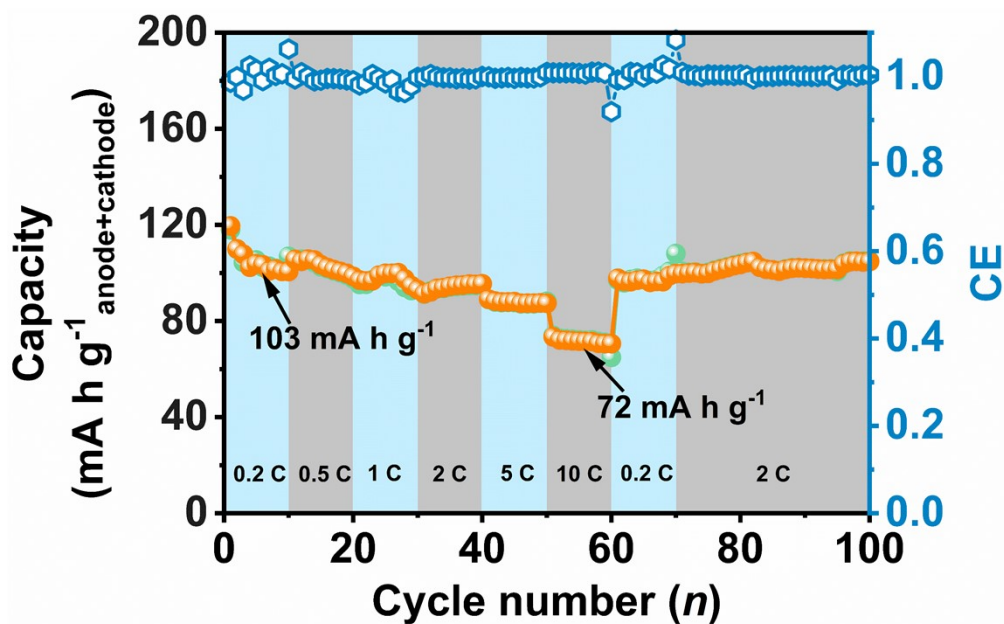


Fig. S16. Rate performance of coin-type full cell in voltage range of 1.0–4.2 V.

The coin-type full cell delivered 103.4, 103.5, 96.6, 94.5, 88 and 72 mA h g⁻¹ at 0.2, 0.5, 1, 2, 5 and 10 C, respectively. After recovering into 0.2 C, the offered capacity can return to the initial level, demonstrating the distinguished rate performance.

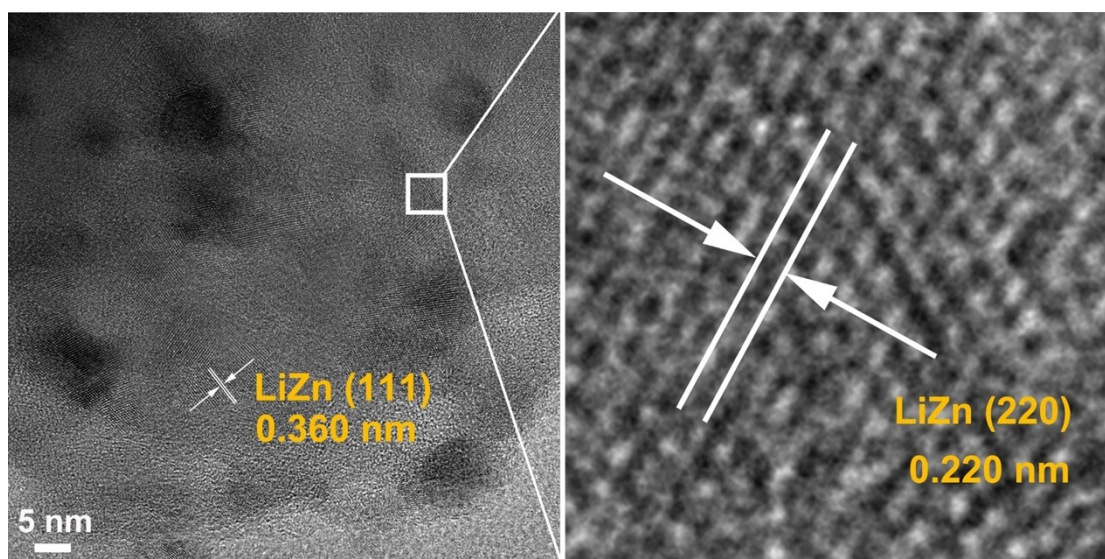


Fig. S17. High-resolution TEM image and corresponded magnified TEM image of ZnO/ZnS electrode after the 1st discharging to 0.01 V.

During the 1st lithiation into 0.01 V, the discharging product crystallizes in LiZn alloy with an average particle size of *ca.* 5 nm and such homogenous particles disperse in Li₂O/Li₂S matrix.

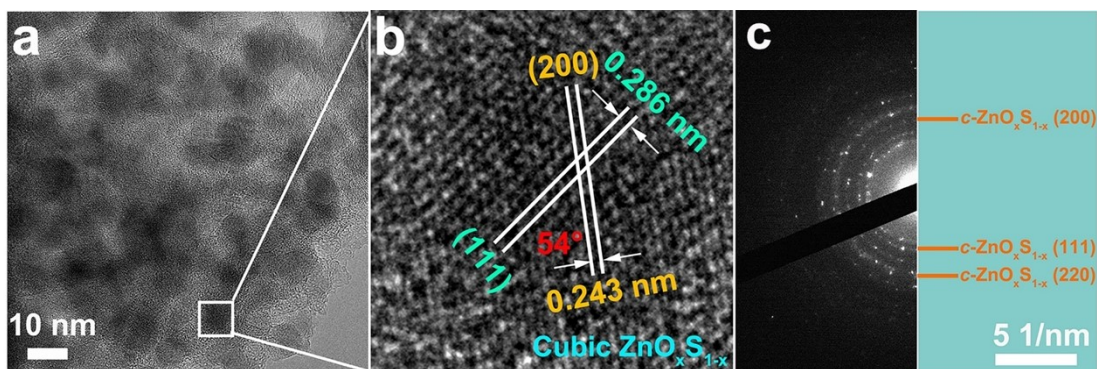


Fig. S18. (a) HRTEM, (b) amplified HRTEM image from selected area in (a), and (c) SAED of ZnO/ZnS electrode after the 1st charging to 3 V.

The lattice spacings of 0.286 and 0.243 nm fall in between the (111) and (200) plane of *c*-ZnO and *c*-ZnS, respectively. The included angle of (110) and (200) plane is 54°, which matches with the theoretical value. Such middle lattice spacing between *c*-ZnO and *c*-ZnS can be considered as the formation of cubic $\text{ZnO}_x\text{S}_{1-x}$, which can also be confirmed by SAED image.

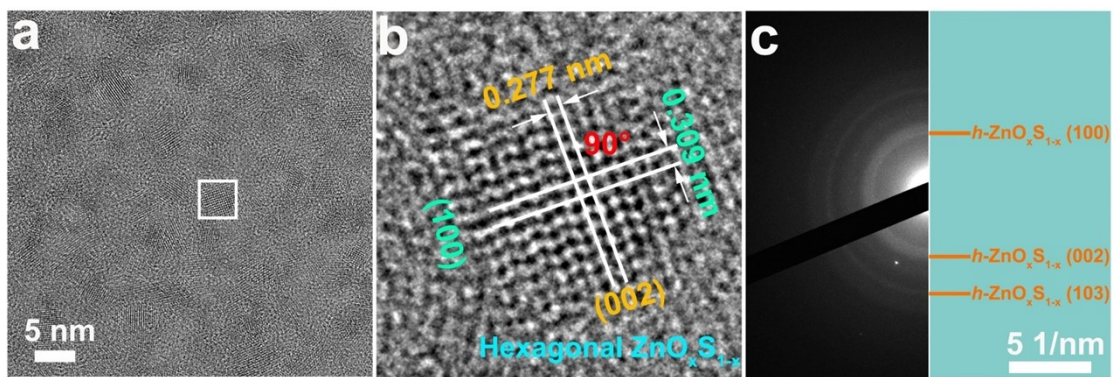


Fig. S19. (a) HRTEM, (b) amplified HRTEM image from selected area in (a), and (c) SAED of ZnO/ZnS electrode after the 2nd charging to 3 V.

The lattice spacings of 0.277 and 0.309 nm with an included angle of 90° refer to (002) and (100) planes of $h\text{-ZnO}_x\text{S}_{1-x}$, respectively. During the 2nd cycle, the $c\text{-ZnO}_x\text{S}_{1-x}$ at the end of the 1st cycle transfers into $h\text{-ZnO}_x\text{S}_{1-x}$. Although HRTEM images reveals several nanocrystals, the overall SAED image contains relatively diffused diffraction ring because of small particle sizes and possible amorphization, suggesting the existence of highly active nanodots.

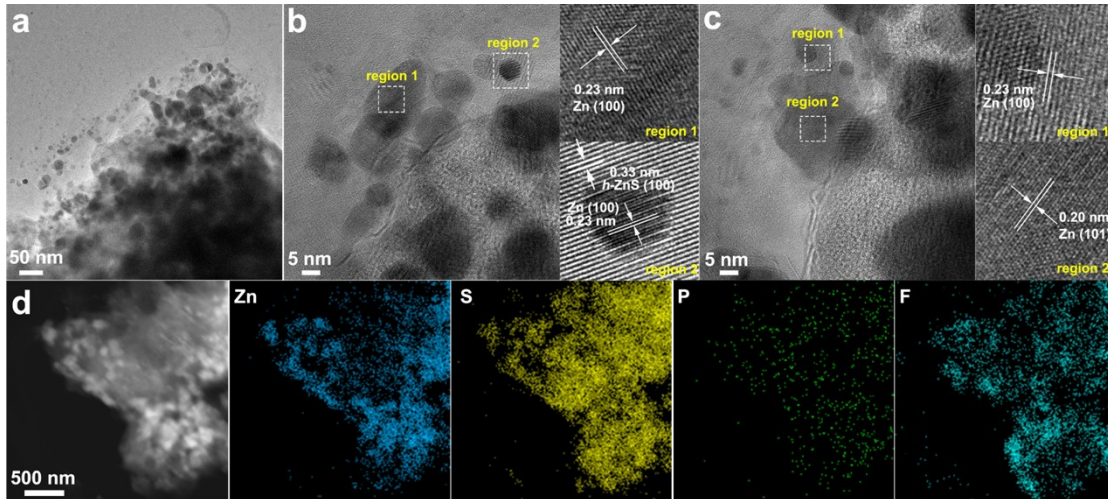


Fig. S20. *Ex-situ* TEM investigations on microstructure of cycled ZnS electrode. **(a)** LRTEM, **(b-c)** HRTEM and **(d)** EDX mapping under HAADF-STEM mode of ZnS after charging to 3 V at the end of the 10th cycle.

For ZnS electrode, the morphology changes from the initial nanosheets (**Fig. S8**) to irregular nanoparticles and the particle size is distributed from 10 to 50 nm (**Fig. S20a**). The resultant particles crystallize in *h*-Zn (PDF#65-3358, $P6_3mc$, $a=b=2.665$ Å, $c=4.947$ Å; $\alpha=\beta=90^\circ$, $\gamma=120^\circ$) and *h*-ZnS (JCPDF#36-1450; $P6_3mc$, $a=b=3.821$ Å, $c=6.257$ Å; $\alpha=\beta=90^\circ$, $\gamma=120^\circ$), as shown in HRTEM images (**Fig. S20b-c**). Interestingly, a core-shell structured *h*-Zn@*h*-ZnS in charging product is discovered in charging product. The lattice fringes are highly matched, which is probably induced by the epitaxial growth of ZnS on *h*-Zn surface during re-conversion process ($\text{Zn} + \text{Li}_2\text{S} \rightarrow \text{ZnS} + 2\text{Li}^+ + 2\text{e}^-$). So, it is not surprising that the phase of charging product phase is transformed from *c*-ZnO_xS_{1-x} to *h*-ZnO_xS_{1-x} for ZnO/ZnS electrode after certain cycles, as discussed in the main text. As depicted in HAADF-STEM images (**Fig. S20d**), the large Zn species in conductive framework (acetylene black) are non-uniformly dispersed. Such large particle size of Zn species would decrease the reversibility.

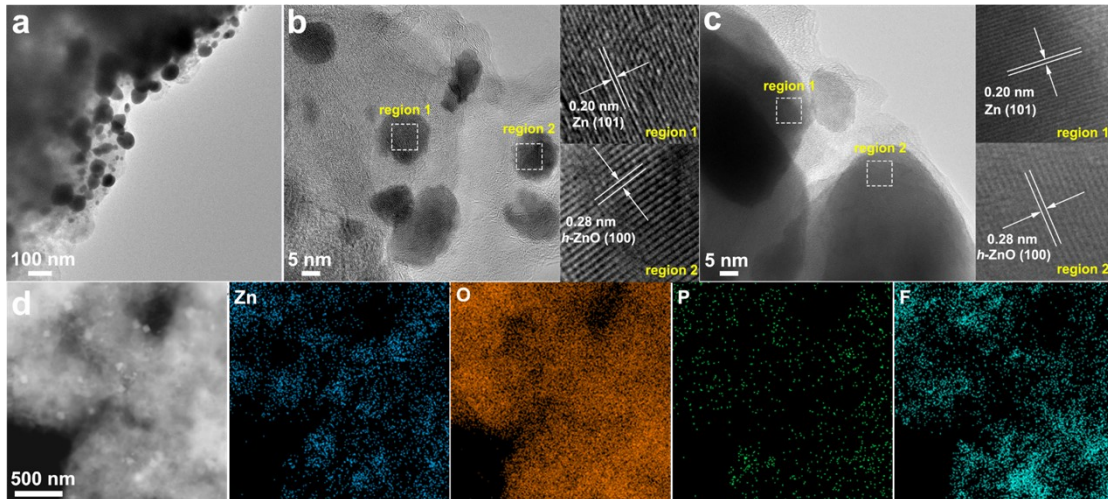


Fig. S21. *Ex-situ* TEM investigations on microstructure of cycled ZnO electrode. **(a)** LRTEM, **(b-c)** HRTEM and **(d)** EDX mapping under HAADF-STEM mode of ZnO after charging to 3 V at the end of the 10th cycle.

Compared with initial morphology and particle size of ZnO (**Fig. S7**), as shown in **Fig. S21a**, the charging product of ZnO electrode exhibits the irregular nanoparticles with uneven particle size distribution from 20 to 100 nm, in which the small particles may be originated from the expansion-induced fracture of large particles. According to the analysis of corresponding HRTEM images (**Fig. S21b-c**), the resultant particles crystallize in *h*-Zn (PDF#65-3358, $P6_3mc$, $a=b=2.665$ Å, $c=4.947$ Å; $\alpha=\beta=90^\circ$, $\gamma=120^\circ$) and *h*-ZnO (JCPDF#36-1451; $P6_3mc$, $a=b=3.250$ Å, $c=5.207$ Å; $\alpha=\beta=90^\circ$, $\gamma=120^\circ$). Ideally, after fully charging into 3V, the electrode would recover into ZnO phase. The existing large *h*-Zn NPs (> 15 nm) illustrates the high irreversibility of ZnO electrode. Although some expected *h*-ZnO can be observed, the large particle size is not favorable for subsequent lithiation/delithiation. Moreover, the HAADF-STEM and EDX mapping (**Fig. S21d**) images display that the large Zn species non-uniformly disperse in conductive agent.

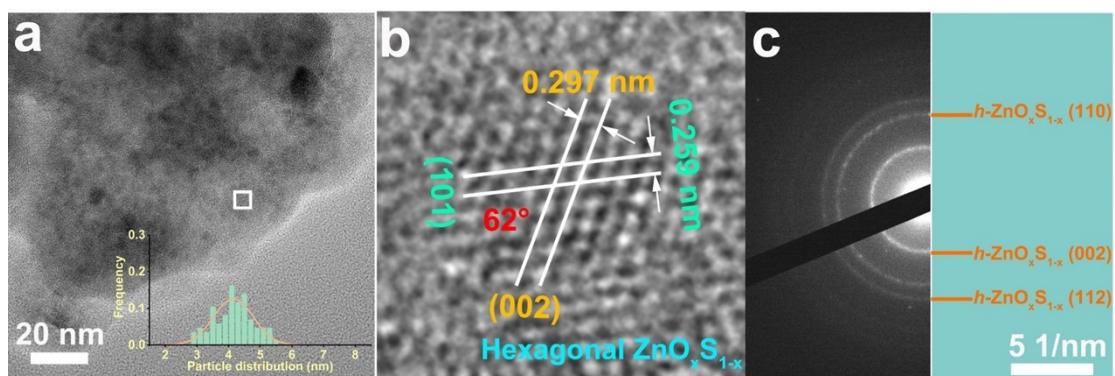


Fig. S22. (a) HRTEM, (b) amplified HRTEM image from selected area in (a), and (c) SAED of ZnO/ZnS electrode after the 20th charging to 3 V.

After recycling into 3 V after the 20th cycle, the particles size of ZnO/ZnS electrode is *ca.* 4.2 nm (**Fig. S22a**). The spacings of 0.297 and 0.259 nm with 62° can be identified as (002) and (101) planes of *h*-ZnO_xS_{1-x}, respectively (**Fig. S22b**). The relatively diffused diffraction ring in SAED image (**Fig. S22c**) further confirms the phase homogenization.

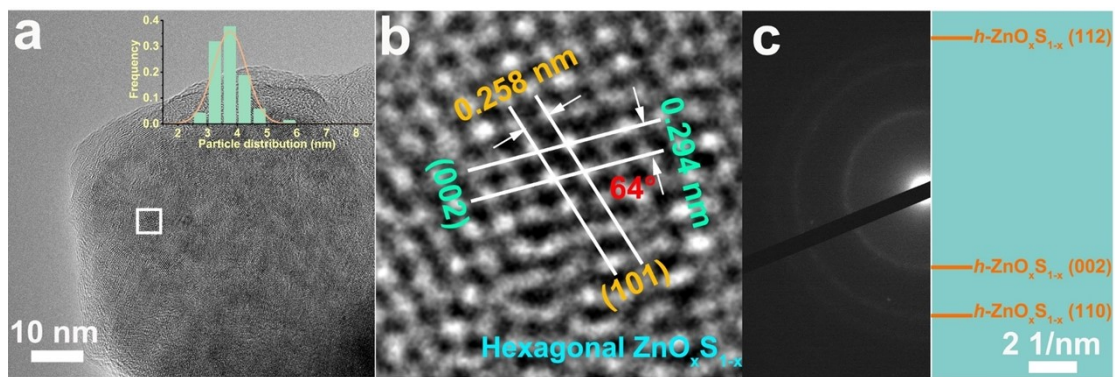


Fig. S23. (a) HRTEM, (b) amplified HRTEM image from selected area in (a), and (c) SAED of ZnO/ZnS electrode after the 40th charging to 3 V.

After the capacity stabilizes in the 40th cycle, the *ex-situ* TEM was carried out, which suggests that the charging product is $h\text{-ZnO}_x\text{S}_{1-x}$ with particle size of *ca.* 3.8 nm (**Fig. S23**). Compared with the microstructure evolution at the 1st, 2nd, 5th, 10th and 20th cycles, the distance between two particles at the 40th cycle is shorter, which is favorable for the Li^+ transfer.

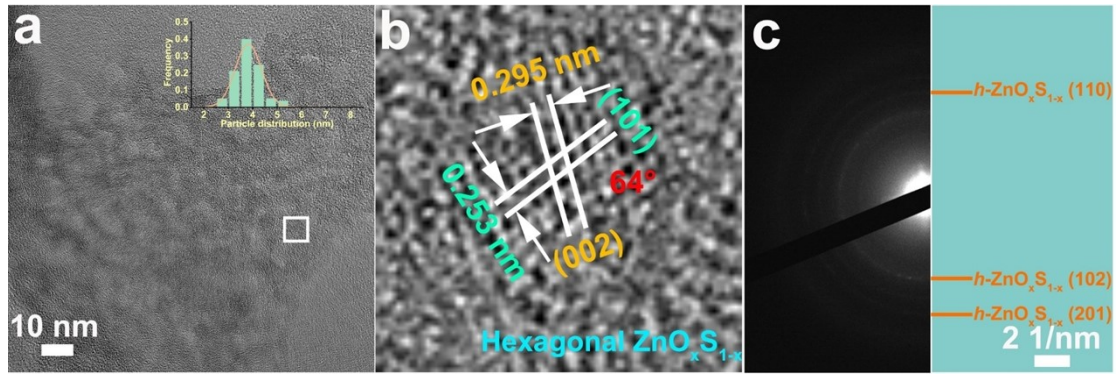


Fig. S24. (a) HRTEM, (b) amplified HRTEM image from selected area in (a), and (c) SAED of ZnO/ZnS electrode after the 50th charging to 3 V.

The average particle size of $\text{ZnO}_x\text{S}_{1-x}$ at the 50th cycle is 3.8 nm, which is the same with that at the 40th cycle. The lattice spacings of 0.295 and 0.253 nm correspond into the (002) and (101) plane of $h\text{-ZnO}_x\text{S}_{1-x}$, respectively. The particle sizes of $\text{ZnO}_x\text{S}_{1-x}$ nanodots at the 1st, 2nd, 5th, 10th, 20th, 40th and 50th cycles are *ca.* 10.1, 3.2, 7.2, 4.9, 4.2, 3.8 and 3.8 nm, respectively. Moreover, according to the cycle performance at 0.1 A g^{-1} , the capacity increases into the maximum value at the \sim 50th cycle and the gradually fades. Therefore, the particle size of $\text{ZnO}_x\text{S}_{1-x}$ would no longer be optimized after 40 cycles.

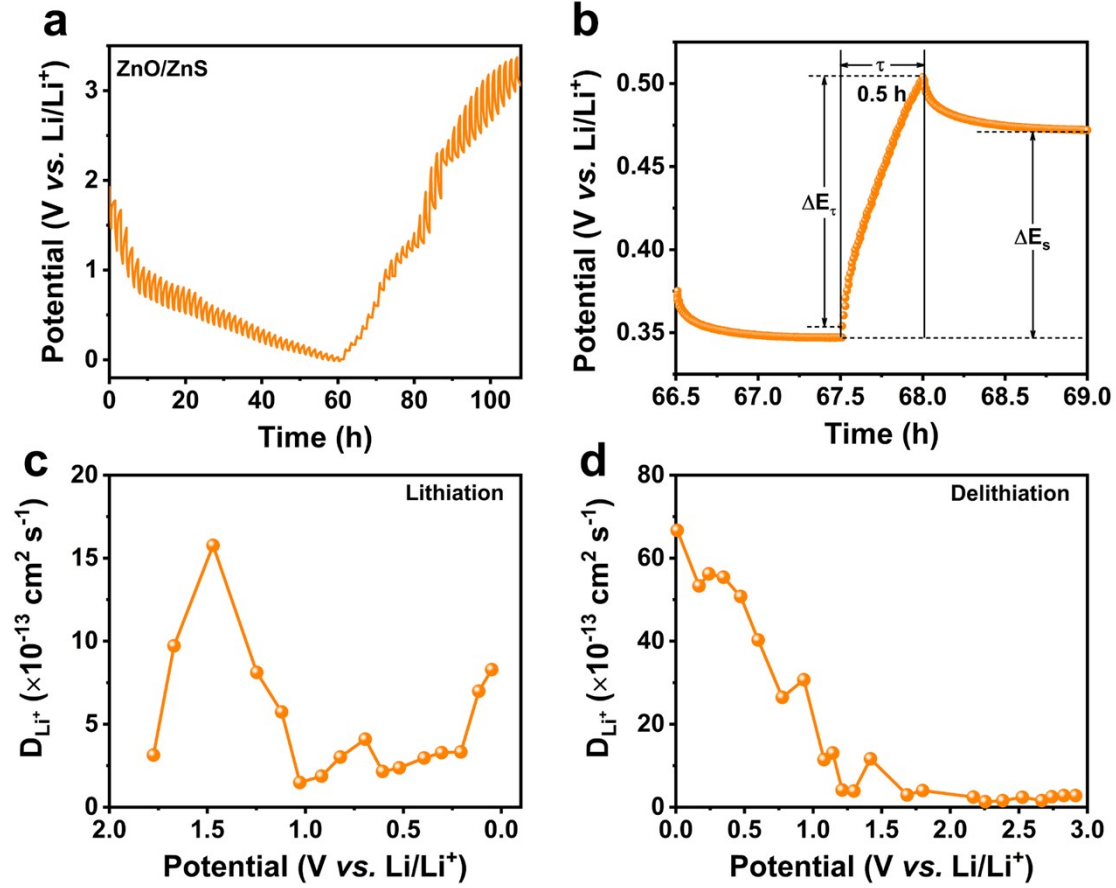


Fig. S25. (a) GITT profiles of ZnO/ZnS at the 1st cycle. (b) The current step diagram at 0.35 V (vs. Li/Li⁺) during delithiation process. The diffusion coefficients of Li⁺ calculated from the GITT profiles during (c) lithiation and (d) delithiation process.

The diffusion coefficient of Li⁺ (D_{Li^+}) was calculated by Fick's second law:

$$D_{Li^+} = \frac{4}{\pi\tau} \left(\frac{m_B V m}{M_B A} \right)^2 \left(\frac{\Delta E_s}{\Delta E_\tau} \right)^2$$

where n , V , and A are the mole of active material, molar volume of active material, geometric area of the electrode, respectively, and E_s and E_τ are defined in Fig. S25b.

We continue the galvanostatic intermittent titration technique (GITT) measurement in the 1st cycle to look into the evolution of the diffusion coefficient of Li⁺ (D_{Li^+}), as shown in **Fig. S25**. The greatest value of D_{Li^+} is 1.6×10^{-12} cm² s⁻¹ during lithiation, when the D_{Li^+} significantly drops from 1.5 to 1.0 V. Then, in the range of 1.0-0.4 V, Li is inserted into the ZnO/ZnS interface to create Zn/Li₂O/Li₂S, and the corresponding D_{Li^+} progressively increases, showing a

fast reaction kinetics. Last but not least, Li alloys with Zn from Zn/Li₂O/Li₂S to generate LiZn/Li₂O/Li₂S. The D_{Li^+} value is, theoretically, substantially smaller during the alloying process than during the conversion process. However, in ZnO/ZnS heterostructure, the situation is reverse and the corresponding D_{Li^+} value gradually increases due to the microstructure evolution and interfacial lithiation storage. During delithiation, the D_{Li^+} value during dealloying process (0.01–0.9 V) is also higher than that during reconversion process (0.9–3 V), confirming the high activity of LiZn nanodots in LiZn/Li₂O/Li₂S. Such high D_{Li^+} value would accelerate the phase construction into ZnO_xS_{1-x}.

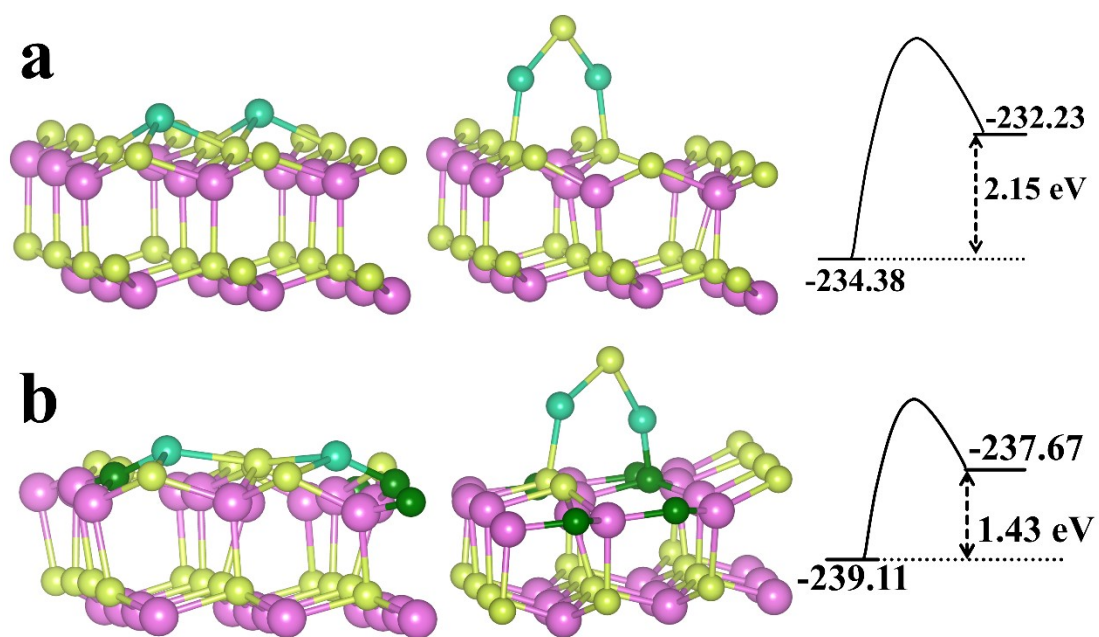


Fig. S26. The formation processes of Li_2S on (a) ZnS and (b) $\text{ZnO}_x\text{S}_{1-x}$ electrodes and the relative energy difference of the formation.

The surface reaction energy of two lithium with one sulfur atom to generate the Li_2S radicals on ZnS and $\text{ZnO}_x\text{S}_{1-x}$ electrodes are compared and the results indicate that the formation of Li_2S on $\text{ZnO}_x\text{S}_{1-x}$ electrode is easier than that on ZnS surface due to the smaller formation heat.

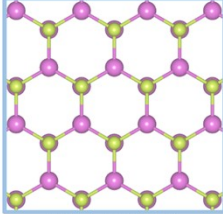
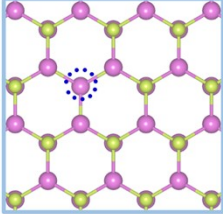

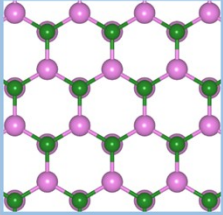
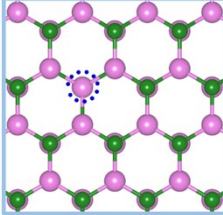

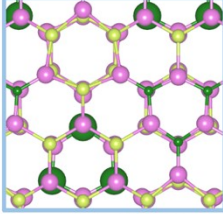
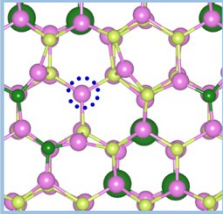

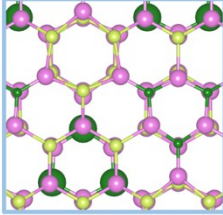
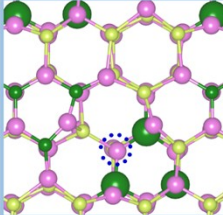

	pristine surface	vacancy surface	atom	E_{form}
a	 -225.46412	 -221.87513	 -0.9099	2.67
b	 -303.69382	 -297.59034	 -1.567	4.53
c	 -234.88803	 -230.88209	 -1.567	2.44
d	 -234.88803	 -231.64125	 -0.9099	2.33

Fig. S27. The vacancy formation energy of S and O at the (a) ZnS, (b) ZnO and (c-d) $\text{ZnO}_x\text{S}_{1-x}$ surface.

The accelerated lithiation reaction to form $\text{Li}_2\text{O}/\text{Li}_2\text{S}$ matrix on $\text{ZnO}_x\text{S}_{1-x}$ electrode can also be understood from the decreased formation energy of S and O vacancies. The calculated vacancy formation energies for O and S of $\text{ZnO}_x\text{S}_{1-x}$ surface are respectively reduced by 2.09 and 0.34 eV in comparison with these on individual ZnO (4.53 eV) and ZnS (2.67 eV), in line with the smaller formation heat of Li_2S .

Table S1. ICP-AES results of two batches of ZnO/ZnS samples.

Sample	Element	Line (nm)	Mean ($\mu\text{g/mL}$)	RSD (%)	Concentration ($\mu\text{mol/mL}$)	S:Zn (atom ratio)
ZnO/ZnS-1	S	182.034	67.2821	0.2235	2.0979	0.8548
	Zn	202.548	160.4873	0.6235	2.4543	
ZnO/ZnS-2	S	182.034	67.5327	1.9731	2.1058	0.8374
	Zn	202.548	164.444	1.1521	2.5148	

Table S2. Peak positions and S $2p_{3/2}$, O $1s$, E_g , and VBM of ZnO, ZnS and ZnO/ZnS.

Sample	Region	BEs (eV)	E_g (eV)
ZnO	O $1s$	530.185	3.25
	VBM	2.09	
ZnS	S $2p_{3/2}$	162.774	3.42
	VBM	1.54	
ZnO/ZnS	S $2p_{3/2}$	162.854	3.22
	O $1s$	530.554	
	VBM	1.97	

S3. References

- [1] X.-Y. Xie, P. Zhan, L.-Y. Li, D.-J. Zhou, D.-Y. Guo, J.-X. Meng, Y. Bai, W.-J. Zhang, *J. Alloys Compd.* **2015**, *644*, 383.
- [2] F. Holtstiege, T. Koç, T. Hundehage, V. Siozios, M. Winter, T. Placke, *ACS Appl. Energy Mater.* **2018**, *1*, 4321.
- [3] J. Hafner, *J. Comput. Chem.* **2008**, *29*, 2044.
- [4] G. Kresse, J. Furthmüller, *Comput. Mater. Sci.* **1996**, *6*, 15.
- [5] J. P. Perdew, K. Burke, M. Ernzerhof, *Phys. Rev. Lett.* **1998**, *80*, 891.
- [6] G.-L. Xu, Y. Li, T. Ma, Y. Ren, H.-H. Wang, L. Wang, J. Wen, D. Millere, K. Amine, Z. Chen, *Nano Energy* **2015**, *18*, 253.